# Band-Stop Behavior Vertically Extended Ground Isolator Based on Transmission Line Theory for IBFD TRx Decoupling Applications

Taeyeong Yoon, *Graduate Student Member, IEEE*, Uichan Park, *Graduate Student Member, IEEE*, and Jungsuek Oh, *Senior Member, IEEE*

***Abstract*— This article presents decoupling methodologies enabling dual-polarized coupling suppression for fifth-generation (5G) sub-6 GHz transmit/receive (TRx) antenna arrays with novel antenna illumination topologies. The isolator comprises the proposed vertically extended bent ground wall, which acts like a multistage band-stop filter modeled as a transmission line, i.e., it has a different behavior from the typical wall structure. To consider dual-polarized multi-path isolations in reliable 5G integration scenarios, an antenna having a height of 0.13$\lambda$ at 3.5 GHz with dual (±45° slant) polarization and port isolation of 25 dB is devised. It was demonstrated that the proposed isolator could significantly suppress the direct and ground coupling between TRx, using the resonance proven by transmission line theory. Moreover, the isolator composite combined with an electromagnetic band-gap (EBG) can further improve their dual-polarized decoupling by removing the surface wave coupling. Two sets of 3.5 GHz 1 × 4 antenna arrays with 45°-slant polarization and the proposed isolator composite were designed, manufactured, and measured for simultaneous decoupling of eight paths among the TRx antenna elements. Finally, the measured results reveal that the overall isolation level of the dual-polarized array configuration is approximately 70 dB with a height of 0.14$\lambda$, maintaining the matching and port isolation conditions.**

***Index Terms*— Array decoupling, dual-polarized antenna, electromagnetic band-gap (EBG), extended bent ground wall isolator, multi-path isolation, mutual coupling, transmit/receive (TRx) isolation.**

## I. Introduction

RECENTLY, wideband and dual-polarization techniques have been used to achieve a high data rate owing to the enormous amount of signal processing required for sub-6 GHz. Based on these requirements, patch antennas [1], [2], [3], [4], [5], [6], metamaterials [7], [8], [9], [10], and crossed dipole antennas [11], [12], [13], [14], [15] are the most commonly used antenna types. In addition, antennas with the abovementioned features have become more prevalent in in-band full-duplex (IBFD) operations to fulfill the demands of wireless communication systems owing to their increased capabilities. Using the same frequency band for the transceiver at the same time, IBFD can double spectral efficiency for future wireless networks, such as the fifth-generation (5G) new radio (NR) [16]. One of the challenges in adequately implementing an earlier advanced scheme using an array antenna is the requirement of mitigating the mutual coupling between the transmitter and receiver (Tx-Rx).

Meanwhile, self-interference, generated from the mutual coupling between Tx and Rx, refers to the interference that a transmitting IBFD terminal brings to itself, which hinders the desired signal from being received by the terminal, as shown in Fig. 1. To recognize the effect of self-interference, we consider the following comprehensive explanations presented in [17] and [18]. The proposed data indicate that the self-interference of the base station is greater than 100 dB above the noise floor when the stations and handsets transmit at 21 dBm with respect to the receiver noise floor. This level is generally obtained using the isolation technology of the propagation, analog, and digital domains. However, in the analog domain, there are many challenges, such as linearity and power efficiency. Therefore, to mitigate and reduce design complexity and cost, a scheme that can skip the analog self-interference cancellation by realizing very high isolation in the antenna domain has been proposed [19]. Hence, in the case of a Tx-Rx array, it is typically necessary to ensure a significant level of isolation for the antennas by employing a suitable isolator. By employing this isolator, the undesirable self-interference is effectively eliminated, resulting in enhanced performance of the IBFD operation. For instance, in [20], a metasurface-based decoupling structure with a large spaced array between the Tx and the Rx was introduced to achieve a high isolation level for bistatic radar systems.

Among the reported approaches for mitigating mutual coupling, decoupling surface using the interaction between direct coupling and the wave reflected by the surface [21], the transmission line-based method [22], [23], resonance patterns [24], [25], [26], metasurfaces [27], [28], resistive films [29], side walls [30], common and differential mode

Manuscript received 21 March 2023; revised 13 June 2023 and 20 July 2023; accepted 23 July 2023. Date of publication 9 August 2023; date of current version 7 February 2024. This work was supported by the Institute of Information and Communications Technology Planning and Evaluation (IITP) through the Korean Government [Ministry of Science and ICT (MSIT)], "Innovative Fusion Technologies of Intelligent Antenna Material/Structure/Network for THz 6G," under Grant 2021-0-00763. *(Corresponding author: Jungsuek Oh.)*

The authors are with the Department of Electrical and Computer Engineering (ECE), Institute of New Media and Communications (INMC), Seoul National University, Seoul 151-742, Republic of Korea (e-mail: taeyeong.yoon@snu.ac.kr; marine522@snu.ac.kr; jungsuek@snu.ac.kr).

Color versions of one or more figures in this article are available at https://doi.org/10.1109/TMTT.2023.3300192.

Digital Object Identifier 10.1109/TMTT.2023.3300192

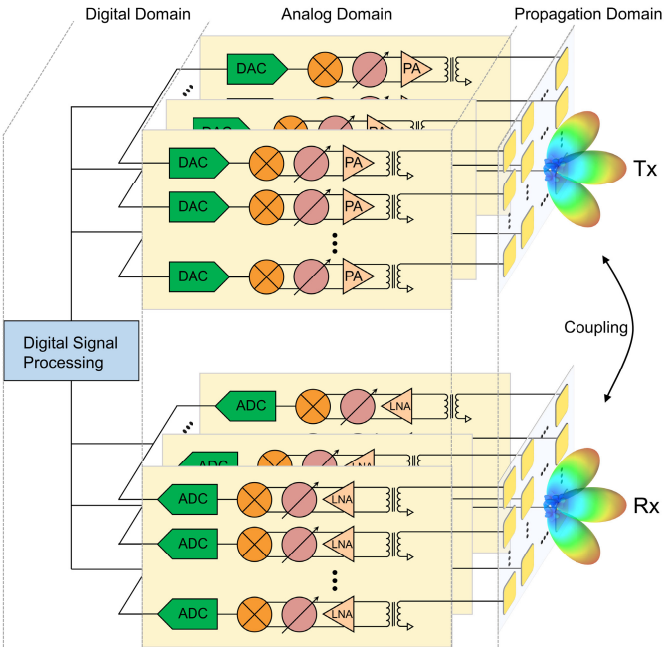


Fig. 1. IBFD transceiver, highlighting the propagation, analog, and digital domains.

cancellation [31], additional coupling paths [32], [33], [34], [35], [36], [37], [38], and electromagnetic band-gap (EBG) [39], [40], [41] are the most effectively used isolator methods. In [42], mutual coupling between dual-polarized array antennas has improved using an array antenna decoupling surface (ADS). Here, the ADS was optimized and designed for single-polarization array antennas and good results were obtained. However, the isolator has some limitations when applied to dual-polarized array antennas. Furthermore, although multiple-input multiple-output (MIMO) systems that use dual-polarization and increase array configurations have recently been in the spotlight, the isolator still has the abovementioned limitations, as revealed in an earlier study. For instance, in [43], an isolation notch was obtained using resonant structure. However, improving all dual-polarized array configurations was difficult. As seen in the results, $S_{25}$ did not have an isolation notch, and $S_{26}$ deteriorated despite the isolator being in use. In addition, in [43], [44], and [45], wall-type isolators have been proposed to mitigate coupling between Tx and Rx elements. However, they implemented the isolator as a simple wall that blocks direct coupling between the elements even though it can be used as a resonance-type isolator based on the proposed analysis in this article. Therefore, here, to reduce the mutual coupling between Tx and Rx using the wall and EBG isolator composite for a dual-polarized array antenna, as depicted in Fig. 2, the coupling paths are first identified. Then, a new effective hybrid structure is presented and demonstrated using the isolator, which has an optimal length for resonance, maintaining a high isolation level with the devised antenna. Specifically, two types of bent-structured wall-type isolators, which act like multistage filters, are presented based on transmission line theory; the isolator and analysis were designed and performed under characteristic symmetrical conditions.

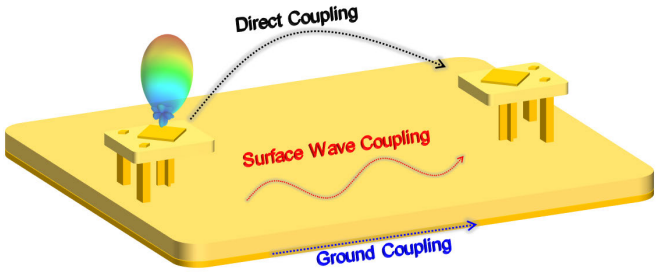


Fig. 2. Schematic of the two-element array and coupling path between the antennas.

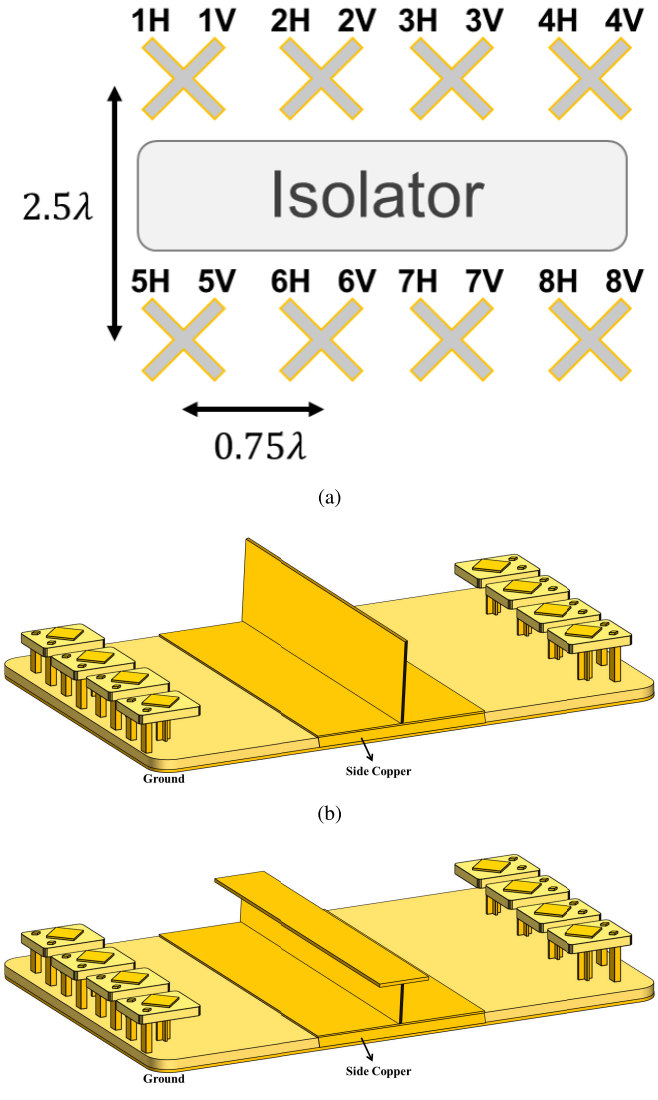


Fig. 3. (a) Layout and numbering scheme of an array configuration for IBFD operation; 3-D view of the single wall: (b) straight and (c) bent.

The rest of this article is organized as follows. The implementation of the isolator enabling generating the resonance based on the transmission line theory is described along with utilizing an EBG for dual-polarized decoupling in Section II. Finally, Section III concludes the study; the illumination of the devised antenna is provided as an appendix.

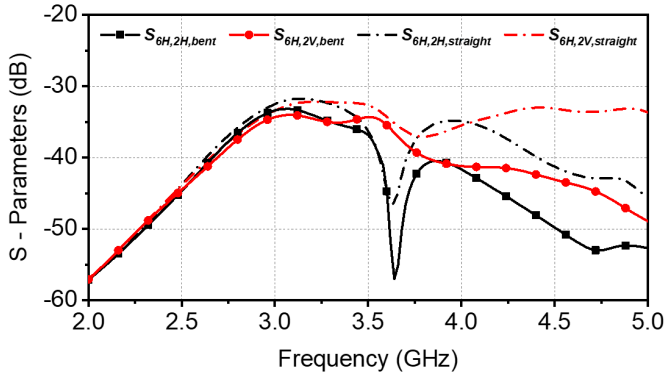


(a)

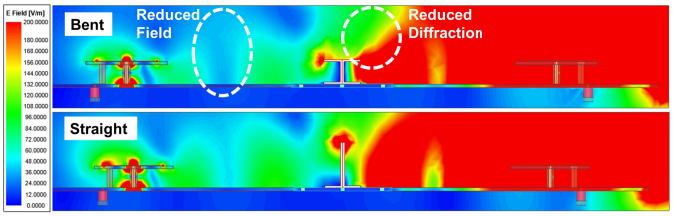


(b)

Fig. 4. Simulated results with respect to the shape of the wall: (a) $S_{6H,2H}$, $S_{6H,2V}$ and (b) electric field distribution.

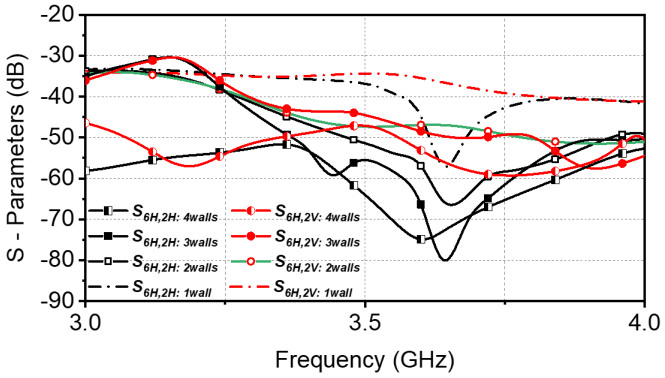


(a)

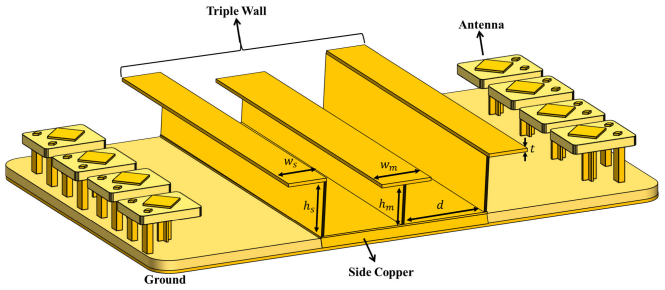


(b)

Fig. 5. (a) Simulated $S_{6H,2H}$, $S_{6H,2V}$ with respect to the number of walls. (b) 3-D view of the system with a wall isolator, where $w_s = 12$ mm, $h_s = 11$ mm, $w_m = 18$ mm, $h_m = 9$ mm, $w_i = 290$ mm, $d = 20$ mm, and $t = 1.5$ mm.

## II. Decoupling Design

This section describes the analysis of the decoupling method of the array antennas for two sets of 1 × 4 antenna arrays using metallic walls. First, the corresponding results were investigated using the electrical-field distributions for straight and bent shapes on a single wall. Thereafter, the results were obtained according to the number of walls, and the optimal number of walls for the system was determined.

The path that causes coupling is analyzed as illustrated in Fig. 2, and the isolator used to implement the decoupling performance is described. Coupling can be analyzed through categorization into direct, surface waves, and ground couplings. This article presents a method for identifying and solving the coupling in dual-polarized array antennas based on this approach.

### A. Wall Analysis

Fig. 3(a) shows the numbering and layout of the Tx-Rx array antenna system. The Tx and Rx were each set with four antennas. Therefore, these are referred to as two sets of 1 × 4 arrays. Antennas belonging to the same set were arranged at a spacing of 0.75$\lambda$; the distance between the sets was 2.5$\lambda$, and isolators were present between them. This study focused on improving the isolation between the upper set (1–4 $H$, $V$) and the lower set (5–8 $H$, $V$). The proposed isolator, employs a metallic wall structure that effectively reduces direct coupling by changing the diffraction. Additionally, the isolator consists of three vertically extended bent ground walls, which are connected to the main substrate's ground through via holes and a copper side. As a result, by utilizing the transmission line analysis method, the isolator functions as a resonant structure: effectively suppressing ground coupling. Fig. 3(b) and (c) illustrate the 3-D models with straight and bent shapes for a single wall isolator, which is the unit structure of the wall isolator. The straight wall height was set to $\lambda/4$ to reduce the ground coupling, and the corresponding analysis is described in Section II-B. Likewise, the height of the bent-shaped wall was determined. Because the physical lengths of the bent and straight shapes must be the same, the bent shape was implemented with a low height, as in the 3-D model illustrated in Fig. 3(c).

The simulation results of $S$-parameters, depicted in Fig. 4(a), illustrate the numerical determination of the coupling level between the Tx and Rx. The presence of a bent structure enhances the isolation for both horizontal and vertical polarizations. These findings can be attributed to the field distribution shown in Fig. 4(b), where the complex magnitude represents results that are independent of time and period. The field passing from Tx to Rx was further induced downward because of the curved edge caused by the bent shape. Therefore, diffraction is suppressed, and the field intensity transmitted to Rx is reduced. In summary, the direct coupling is mitigated by reducing diffraction in the 3-D structure of the wall, and the isolation level is effectively improved by the bent structure, which can reduce the height of the isolator also. In addition, the ground coupling is enhanced by modeling the wall as a transmission line and using a resonant structure, which will be described in detail in Section II-B.

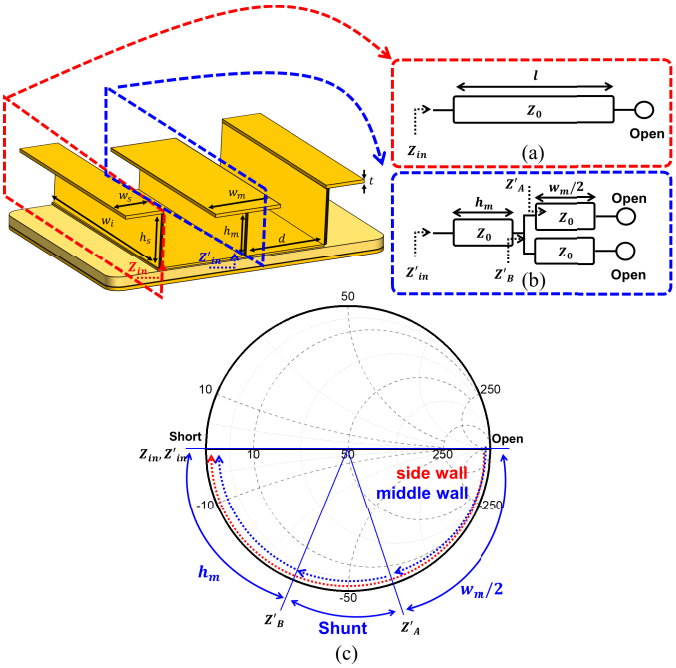


Fig. 6. Description of the input impedance of a single wall analyzed as a transmission line: (a) side wall, (b) middle wall, and (c) Smith chart traces of each wall.

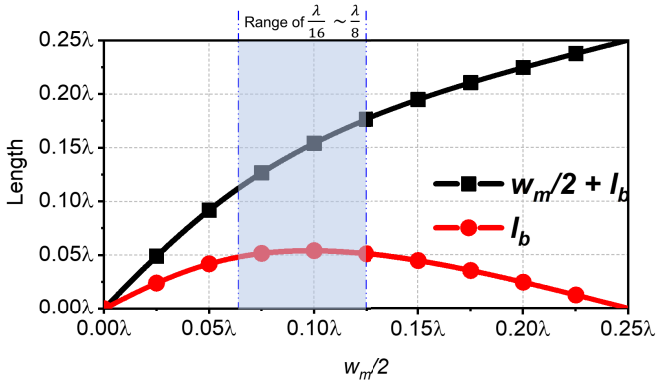


Fig. 7. Results of the effective length by the shunt impedance decrease.

Fig. 5(a) presents the results obtained by increasing the number of walls for each polarization. Intuitively, the number of walls in the isolator is significant because the walls can block direct coupling and prevent ground coupling simultaneously while adjusting the appropriate length of the wall. The black line represents the result of the same polarization when the number of walls increases, and the red line represents the coupling result of the two antennas with different polarizations. When considering the coupling between antennas with the same polarization, the isolation-level proportionally has improved as the number of walls increases. This tendency was also observed in the coupling results of the antennas with different polarizations. However, when the number of walls is three or more, the isolation level does not improve significantly. Therefore, considering the area occupied by the isolator, the optimum number of walls to be used was three. Fig. 5(b) illustrates the wall isolator's 3-D model and dimension parameters determined based on Section II-B.

### B. Wall With Transmission Line Theory

Because the presented distance condition among the array set is sufficiently large, the isolator satisfies the far-field condition. Thus, the isolation wall can be modeled as a transmission line, as illustrated in Fig. 6(a) and (b), because the wave on the ground is a quasi-TEM. The input impedance of the side wall, based on the transmission line theory of the wall, is as follows [46]:

$$Z_{\text{in}} = Z_0 \frac{Z_L + jZ_0 \tan \beta l}{Z_0 + jZ_L \tan \beta l} \tag{1}$$

$$l \approx h_s + w_s \tag{2}$$

$$Z_{\text{in}} = \frac{Z_0^2}{Z_L} \tag{3}$$

where $Z_0$ and $Z_L$ are the characteristic and load impedances of the wall, respectively. Moreover, the line length is approximately represented by (2) because the wall's height can be modeled as a transmission line. Here, (3) is obtained if $l$ is a quarter-wavelength. From the equation, $Z_{\text{in}}$ can exhibit a significantly low impedance when the load is an open circuit (OC) ($Z_L \approx \infty$), and the condition $Z_0 \ll Z_L$ holds true, which is ensured by having a sufficiently wide wall with $w_i = 290$ mm [47]. As a result, the impedance of the wall can be extremely low, similar to a short circuit. Fig. 6(a) and (b) show different interpretations of the side and middle walls. The middle wall is composed of a T-shape for the structural symmetry of the isolator; therefore, it is modeled as a shunt transmission line with $w_m$ length and connected to the transmission line with $h_m$ length. Fig. 6(c) shows the operation of the shunt line for each node. Interestingly, unlike the side wall, it satisfies the equation below because the shunt line decreases the additional impedance

$$\frac{w_m}{2} + l_b + h_m = \frac{\lambda}{4} \tag{4}$$

where $l_b$ is the effective length of the impedance decrease by the shunt transmission line, which is identical to the shunt range in Fig. 6. Furthermore, (4) can be simplified under the conditions that $w_m/2 = h_m = \phi$ and $l_b \approx \lambda/20$. The approximation of $l_b$ could be explained by an effective length from the shunt impedance decrease. The impedance is obtained by (1) with $Z_0 \ll Z_L$ and calculated as below

$$Z'_A = \frac{Z_0}{j \tan \beta \frac{w_m}{2}} \tag{5}$$

$$Z'_B = \frac{Z_0}{j2 \tan \beta \frac{w_m}{2}} = \frac{Z_0}{j \tan \beta (\frac{w_m}{2} + l_b)} \tag{6}$$

the effective length by the shunt impedance decrease can be induced using the impedance calculated by (6)

$$\frac{w_m}{2} + l_b = \frac{1}{\beta} \arctan \left( 2 \tan \beta \frac{w_m}{2} \right) \tag{7}$$

the result of (7) is illustrated in Fig. 7. Here, the condition of $\lambda/16$ to $\lambda/8$ range for $w_m/2$ is determined to maintain the constant shunt impedance decrease. As a result, $l_b$ can be approximated by $\lambda/20$ as shown in Fig. 7. In addition, the modified result about $\phi$ is given below

$$\phi \approx \frac{\lambda}{10}. \tag{8}$$

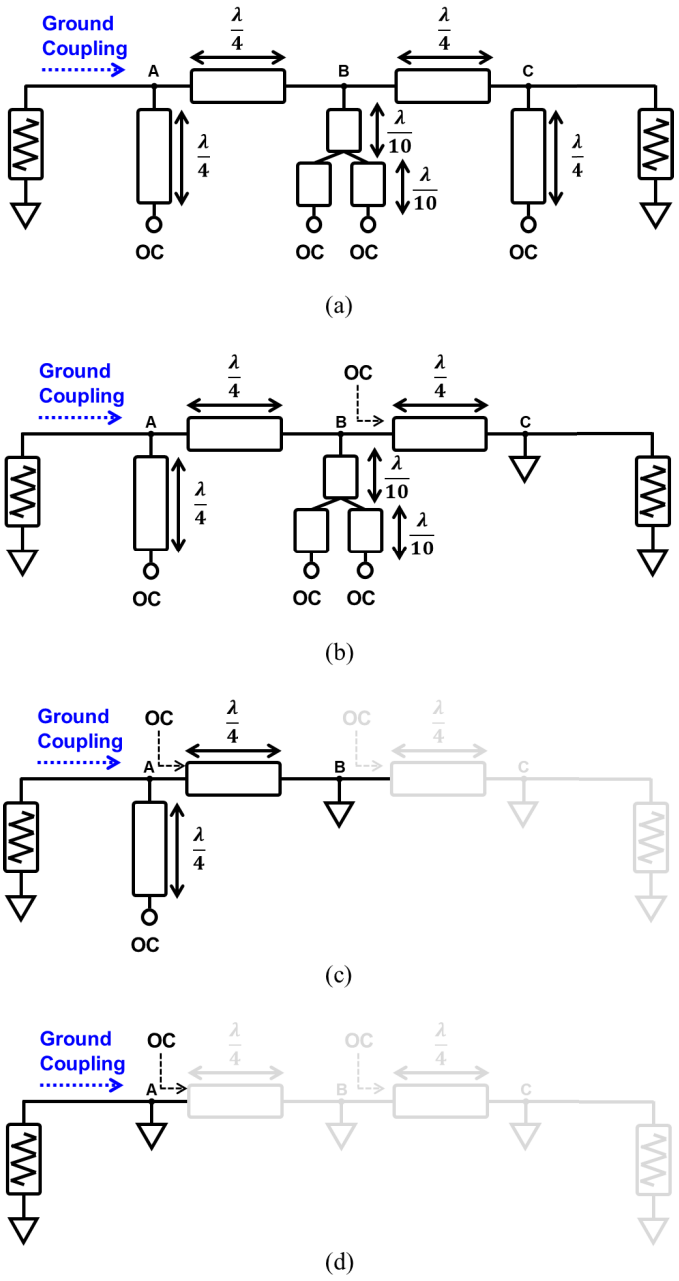


Fig. 8. Schematic and analysis of (a) triple-wall based on transmission line theory; for node (b) C, (c) B, and (d) A.

Accordingly, the dimensions of the middle wall are properly determined for resonance and must be smaller than the side wall. Consequently, the corresponding wall height can minimize the input impedance because the end edges of the wall are considered OCs. This is because the end of the line is in contact with air, which has an intrinsic impedance of $120\pi$ (377 Ω).

Fig. 8(a) shows the operating principle of the wall isolator, and ground signal flows based on transmission line analysis. Each wall can be interpreted as a signal line through which the ground coupling passes, and the height and spacing of the walls are modeled as transmission lines. To begin the analysis in the process depicted in Fig. 8(a), the nodes where each line crosses are denoted by A, B, and C, respectively. When the line

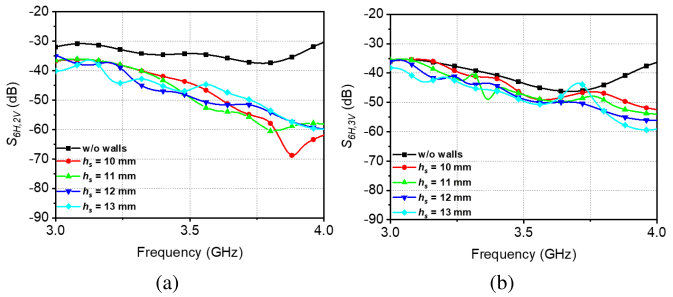


Fig. 9. Simulated results with respect to different $h_s$ values: (a) $S_{6H,2V}$ and (b) $S_{6H,3V}$.

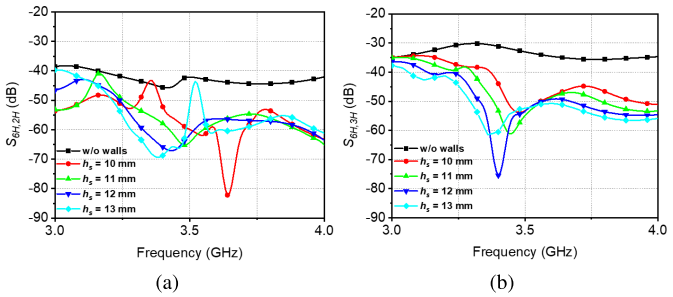


Fig. 10. Simulated results with respect to different $h_s$ values: (a) $S_{6H,2H}$ and (b) $S_{6H,3H}$.

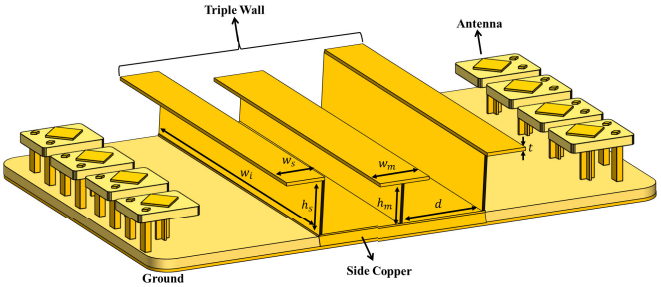


Fig. 11. 3-D view of the system with walls and EBG, where $w_s$ = 12 mm, $h_s$ = 12 mm, $w_m$ = 18 mm, $h_m$ = 9 mm, $d$ = 20 mm, $t$ = 1.5 mm, $w_e$ = 11.6 mm, $s_e$ = 1 mm, and $sp_e$ = 12 mm.

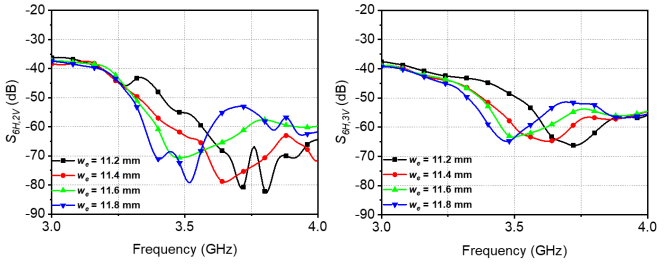


Fig. 12. Simulated results with respect to different $w_e$ values: (a) $S_{6H,2V}$ and (b) $S_{6H,3V}$.

length from node C is $\lambda/4$, based on transmission line theory, it becomes a short circuit as shown in Fig. 8(b). Subsequently, it can be interpreted as an OC when looking at node C from node B because the spacing of the walls is $\lambda/4$ as illustrated in Fig. 8(c).

Moreover, the line of node B whose length is $\lambda/5$ becomes a short circuit, as shown in Fig. 6(c). Subsequently, as shown in Fig. 8(d), the same process is followed for nodes B and A. Finally, a short circuit exists in node A such that all ground coupling is induced to the walls by the low impedance, which improves the isolation level. In summary, if metallic walls are

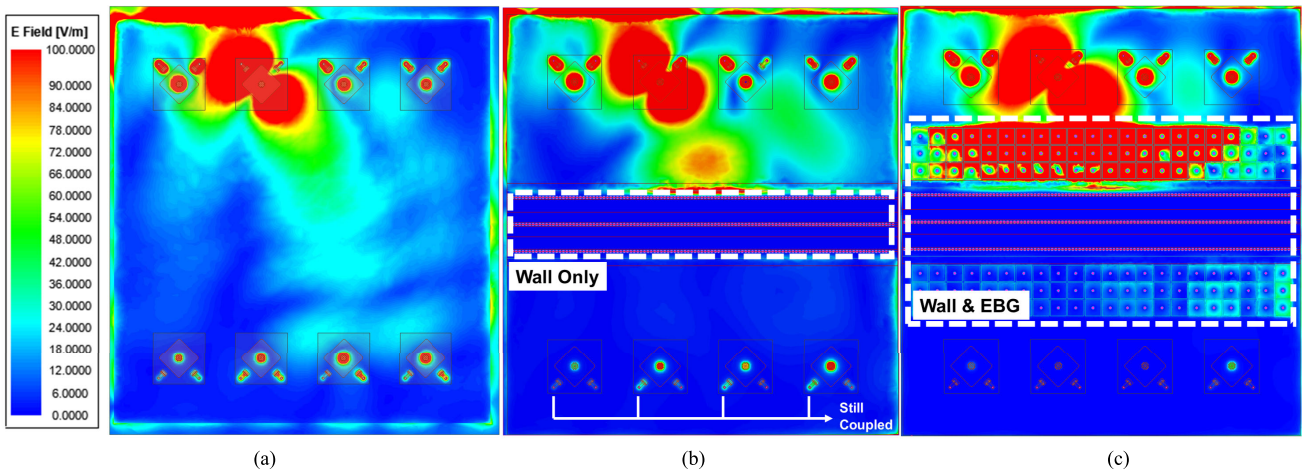


Fig. 13. Electric field distribution of the array antenna system: (a) without the isolators, (b) with the wall, and (c) with the wall and EBG.

used to realize the wall isolator, the direct coupling can be intuitively removed. If the appropriate length and spacing are used when the walls are connected to the ground directly through the side copper or via holes: the operation of the isolator can also be used as ground coupling suppression that acts as a resonance structure.

Before discussing the analysis, we explain the overall results based on a representative analysis of $S_{6H,2H}$, $S_{6H,2V}$, $S_{6H,3H}$, and $S_{6V,3V}$ rather than analyzing each antenna and polarization. Fig. 9 shows the results for $S_{6H,2V}$ and $S_{6H,3V}$. The overall isolation levels have improved by the addition of metallic walls. However, the variation in the resonance point with respect to the adjustment of $h_s$ is not clear and irregular. This means that the ground coupling suppression does not work well for the polarization, and the wall isolator only suppresses the direct coupling. Thus, an isolation level of approximately 50 dB was obtained in the absence of an isolation notch owing to the wall at 3.5 GHz. By contrast, as illustrated in Fig. 10, isolation notches owing to the wall type isolator have improved the decoupling level at the target frequency. The results indicate that the resonance frequency of the isolation notch caused by the isolator decreases as $h_s$ increases because the increase in $h_s$ leads to an increase in the electrical length of the metallic wall, as depicted in Fig. 8, i.e., decreasing the resonance frequency. In other words, the horizontal polarization results presented in Fig. 10 indicate that the isolator using the walls not only suppresses the direct coupling but also effectively suppresses the ground coupling through the resonance structure, unlike the result in the case of the vertical polarization presented in Fig. 9.

Finally, for the coupling results from the vertical to horizontal polarization, it can be predicted that there is no significant improvement by suppressing the ground coupling and direct coupling using the isolator because of the continued existence of surface wave coupling. By contrast, a highly improved isolation level can be obtained by suppressing the ground and direct couplings for identical polarizations.

### C. Wall With EBG

To understand why different results for the polarizations correspondence identified above were obtained owing to

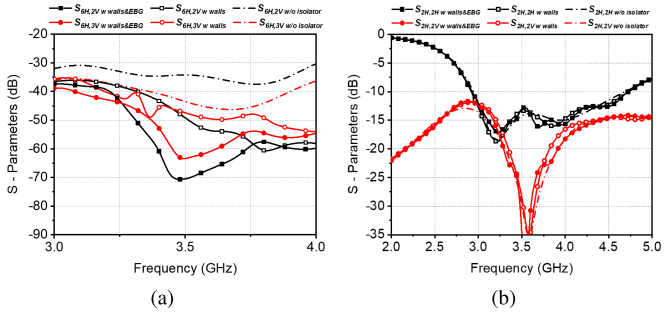


Fig. 14. Simulated results with respect to the presence of an isolator: (a) coupling and (b) matching.

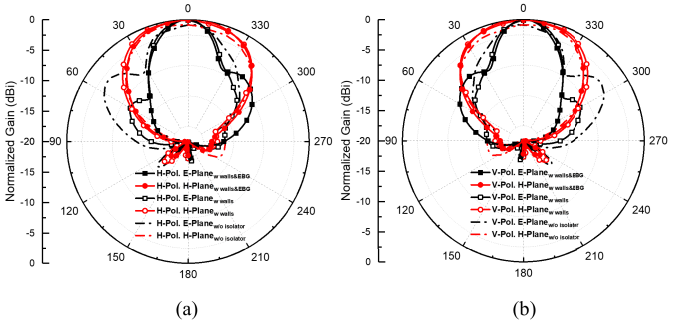


Fig. 15. Beam patterns ($E$- and $H$-plane) obtained in the simulation with respect to the presence of the isolator: (a) horizontal and (b) vertical polarization.

the surface wave coupling, an EBG that suppresses surface waves was introduced. To adequately anticipate the stopband characteristic for the surface wave coupling, a full-wave analysis using ANSYS HFSS is required. In the structure with 2-D periodicity using the unit cell symmetry, a dispersion diagram depicting the energy band of the EBG was obtained. Therefore, the unique propagation vector was grouped in a region referred to as the irreducible Brillouin zone [48]. Based on the concept, it is seen that there is a band gap in which energy does not exist, and the surface energy analysis indicates that the corresponding part will play a role in suppressing the surface wave. Fig. 11 illustrates the isolator arrangement, a wall structure that suppresses the direct and ground couplings and the EBG, which suppresses the surface wave coupling. The EBG was planted on the main substrate, which shared

the ground among the array antenna sets, and a square patch was connected to the ground through via holes.

Fig. 12 presents the results of $S_{6H,2V}$ and $S_{6H,3V}$ for the situation using walls and EBG. In contrast to earlier results regarding the coupling between horizontal polarization, adjustable isolation notches were observed, and the isolation level has improved significantly. The isolation notches can be shifted by adjusting the EBG patch width. The results indicate that the resonant frequency decreased as the patch width increased, and advanced results can be obtained at the target frequency through optimization using this process. The results obtained in the presence of each isolator are presented in Fig. 13, where the electric field is plotted. Fig. 13(a)–(c) display the field in the absence of an isolator, with walls only, and with walls and EBG, respectively. However, as the field intensity of the lower set's ports, they are still excited by the surface wave (i.e., there is an isolation degradation even though the wall isolator reduced the overall field distribution). This problem has been managed using EBG, and the coupling of the lower set was completely removed, as implied by the electric field distribution presented in Fig. 13(c).

As shown in Fig. 14(a), when there was no isolator, the isolation level had a value of approximately 40 dB for the vertical polarization, and when only the wall isolator was used, the isolation level improved by approximately 50 dB. However, the effect of the intended resonance structure was not observed. When walls and EBG are used together, an isolation notch can be made, and the isolation level improved to approximately 65 dB. In addition, as illustrated in Fig. 14(b), it can be confirmed that the matching conditions were maintained depending on the presence of each isolator. Furthermore, Fig. 15 depicts the antenna beam patterns for the *E*- and *H*-planes. The half-power beamwidth (HPBW) was reduced by approximately 10°, and gain is enhanced by about 1 dB by introducing isolators because the wall isolator can be considered as PEC reflector (i.e., the reflected wave is combined as an in-phase). Although the HPBW decreased, the gain increased correspondingly. Therefore, that channel capacity can be expected to improve based on Shannon's theorem.

### *D. Measurement and Analysis*

The designed antenna and isolator were measured using an MS4647 vector network analyzer in an anechoic chamber. As shown in Fig. 16, the other ports except for the two ports for measurement were terminated; measurements were carried out. In addition, because the system had a very sensitive isolation level, an absorber was placed between the structure and the vector network analyzer owing to the coupling caused by the reflection. To ensure consistent and accurate outcomes for this highly sensitive system, which is prone to errors, we maintained the calibration level at around −60 dB throughout the measurement process. Additionally, we enhanced the reliability of the results by maximizing the output power of the vector network analyzer.

Fig. 17(a) presents the results of the simulated coupling of the dual-polarization array antenna following the optimization.

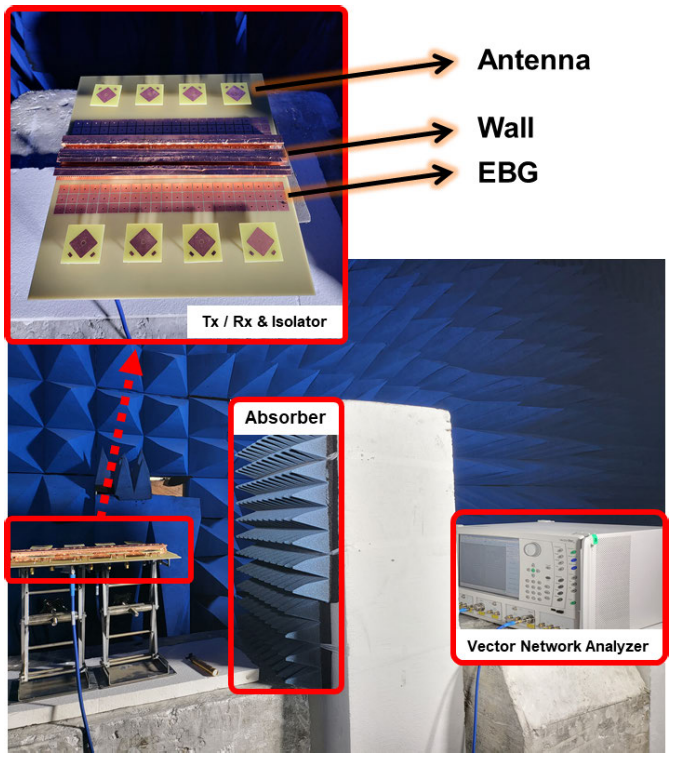


Fig. 16. Fabricated antennas with the isolator composite and measurement setup.

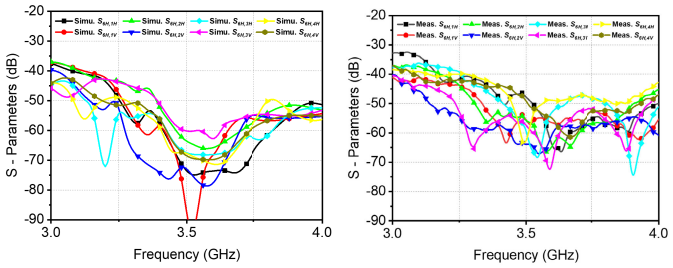


Fig. 17. Results of the (a) simulation and (b) measurement of *S*-parameters for all array antennas.

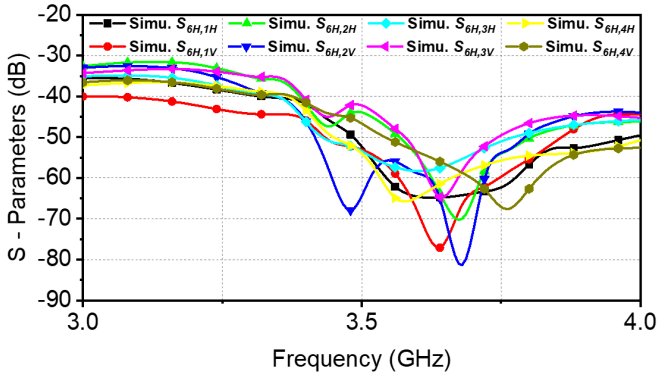


Fig. 18. Results of simulation under practical conditions.

Eight results indicate the coupling of the four dual-polarized antennas of the upper set to the lower antennas. Therefore, the isolation notches can be created at the target frequency if the previously suggested method uses two resonance structures of vertical and horizontal polarization. Fig. 17(b) indicates that isolation notches occurred at the target frequency for the

TABLE I
PERFORMANCE COMPARISON TABLE

| Ref. | Array config. | Array spacing ($\lambda$) | Isolation improvement (dB) | Pol. | Antenna design | Antenna size ($\lambda^3$) | Height ($\lambda$) |
|---|---|---|---|---|---|---|---|
| [20] | 1×2 | 3.0 | 20 | dual | yes | 3×3×4 | 4 |
| [21] | 4×4 | 0.5 | 15 | dual | yes | 0.28×0.28×0.18 | 0.4 |
| [22] | 4×2 | 0.5 | 20 | single | no | 0.35×0.35×0.07 | 0.07 |
| [44] | 1×2 | 1.2 | 10 | dual | yes | 0.35×0.35×0.09 | 0.11 |
| [49] | 3×3 | 0.5 | 20 | dual | yes | 0.35×0.19×0.19 | 0.51 |
| This work | 2×4 | 2.5 | 25 | dual | yes | 0.28×0.28×0.11 | 0.14 |

measurement. However, in contrast to the simulation results, we observed that the notches were distributed within a narrow band with an error of approximately 5%. This discrepancy can be attributed to misalignment issues during the manual manufacturing of the antenna and isolator. It is likely that each antenna underwent rotational misalignment around an axis perpendicular to the substrate plane due to the aforementioned reasons. Furthermore, since this manufacturing issue affects both the antenna and isolator, it was taken into account during the simulation process, as depicted in Fig. 18. The simulation considered a scenario where each antenna and the wall isolator were rotated by ±5° with respect to the axis perpendicular to the substrate plane. As a result, the isolation notches exhibited an error of approximately 5% compared to the target frequency, in contrast to the results shown in Fig. 17, which assumed ideal conditions. In summary, the error on the sensitive system was minimized by performing a new calibration each time the calibration measurement port was changed and maximizing the output power of VNA. The simulation reflecting the manufacturing error indicates that the measurement results were within a reasonable range. A comparison of the performance of the isolators used in various studies is presented in Table I. Here, isolation improvement in the table means that the value is the relative level in isolation with and without each proposed isolator based on the data provided in the reference papers. In addition, the height in the table indicates the vertical length of the system, including both antennas and isolator. Although several researchers have found it challenging to improve the isolation for horizontal and vertical polarizations, this study effectively analyzed the coupling path and obtained improved results for all polarizations and array antennas. Table I indicates that in addition to high isolation improvement and the isolator has low-height characteristics because of its bent shape.

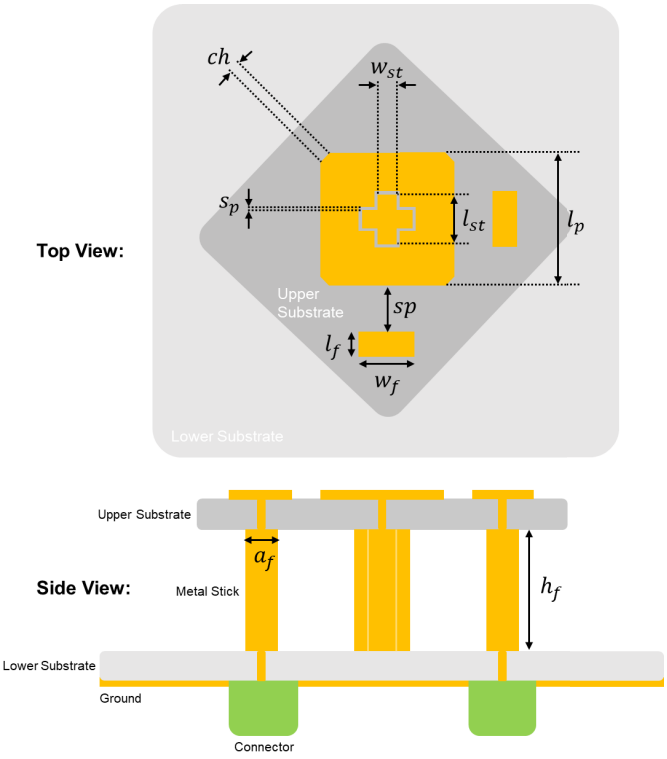


Fig. 19. Configuration of the proposed antenna with versatile metal sticks. The designed geometric parameters are: ch = 1.41 mm, $w_{st}$ = 2 mm, $s_p$ = 0.4 mm, $l_{st}$ = 4 mm, $l_p$ = 21 mm, sp = 2.5 mm, $l_f$ = 3 mm, $w_f$ = 5 mm, $a_f$ = 2 mm, and $h_f$ = 9.5 mm.

## III. CONCLUSION

We proposed a novel approach to analyze metallic walls for decoupling dual-polarized array antennas, utilizing transmission line-based bent walls. Our study involved the implementation of a self-designed antenna within an array for the decoupling system. We examined three potential paths to address the coupling issue and introduced a structure for suppressing coupling in each path. The wall isolator effectively blocks direct coupling and can also mitigate ground coupling by adjusting the wall length to achieve resonance characteristics. As a result, the horizontal polarization of the dual-polarized antennas has been significantly improved, although further enhancements are required for vertical polarization. We identified surface wave coupling as a cause for the vertical polarization problem, which the wall isolator alone cannot suppress. To address this, we combined the walls with an EBG structure to eliminate surface waves. Consequently, the issue of vertical polarization was successfully resolved, resulting in an isolation level of approximately 65 dB for the dual-polarized array antenna. Our proposed design overcomes a significant limitation in the application of the dual-polarized array system to IBFD's transmit/receive (TRx) operation and provides a viable solution for constructing a high-performance system.

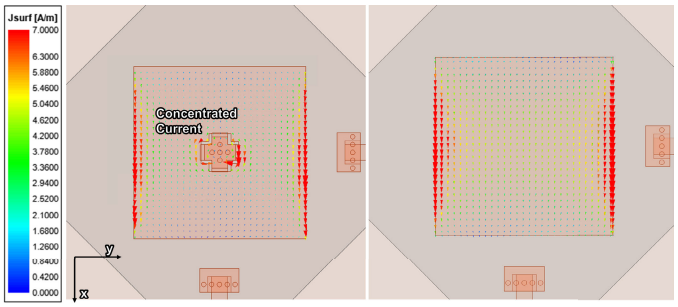


(a) (b)

Fig. 20. Current distribution on the radiating patch: (a) with metal stick and (b) without metal stick.

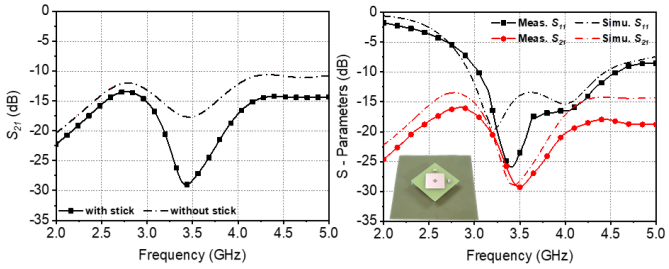


(a) (b)

Fig. 21. Results of (a) simulated effect of the floating metal stick on $S_{21}$ and (b) simulated and measured *S*-parameters with the fabricated model.

## APPENDIX

### A. Antenna Design

A dual-polarization characteristic and a high level of port isolation are required for pure linearly polarized radiation to free space. As explained in [50], concentrating current on the radiation patch is a method for obtaining high levels of port isolation, as the polarization is related to an induced current at the center of the patch in the $TM_{10}$ mode. Side and top views of the proposed antenna are shown in Fig. 19. Two thin FR-4 substrates are used: the upper one is used for laminating the coplanar feeding network and radiation patch, and the lower one is used for the ground and connectors. In addition, there are three metal sticks, two of which facilitate the efficient usage of the feeding network using an air-filled substrate. The third one is used to obtain high port isolation from the concentrated current on the patch. The feeding network on the upper substrate is connected to the side metal sticks through via holes. The cruciform slot of the patch is also connected to the middle stick through via holes.

Fig. 20(a) and (b) shows the current concentration in the middle stick. The figures display the current distribution on the upper substrate, including the radiation patch and feeding network. Fig. 20(a) and (b) shows the result with and without the isolation metal stick, respectively. For the simulation, the *x*-axis polarization port is excited. The current is generated relatively strongly in the middle of the patch. Here, the *x*-axis polarization current is in the same direction. Meanwhile, the *y*-axis polarization current flows in the opposite direction. Therefore, the port isolation is improved because the *y*-axis current is canceled in the far-field, while the *x*-axis current is concentrated in the middle of the radiator. Port isolation using current concentration can be controlled using the dimensions of the stick. The isolation notch of the antenna can be lowered by increasing the middle stick's size because the current path is related to the resonant frequency through the wavelength.

Moreover, it is necessary to float the stick for current concentration from the ground to maintain the voltage at the center of the radiator. In [51], numerical analysis was conducted to prove the relationship between the bandwidth and characteristics of the substrate. Considering the equation and results of this relationship, a thick and lowest-permittivity substrate is required to improve the bandwidth. Therefore, an air-filled substrate is proposed here. Typical substrates have a standard thickness and permittivity greater than 1. These limitations curtail the antennas' bandwidth. However, they can be overcome using an air-filled substrate with no thickness restrictions and a permittivity of 1. This can be achieved through the two side metal sticks, as shown in Fig. 19 (side view), because the metal sticks not only excite the patch but also fix the upper substrate. A coplanar capacitive feeder is used with sticks connected through via holes. The small rectangular copper traced on the upper substrate, shown in Fig. 19, indirectly excites the path for bandwidth improvement [52].

### B. Experimental Results

The proposed antenna exhibited wideband dual-polarized characteristics due to the combination of metal sticks and a radiator. Fig. 21(a) reveals the effect of the current concentration implemented using the floating metal stick on the port isolation ($S_{21}$). When the metal stick was absent, it had an isolation level of approximately 15 dB. However, in its presence, the performance was improved by 30 dB at 3.5 GHz. To verify the design, a fabrication of the proposed antenna is used [see Fig. 21(b)]. The *S*-parameters ($S_{11}$, $S_{21}$) were measured using MS4647 vector network analyzer. The radiation pattern measurements were conducted in an anechoic chamber. The results of the measurement and simulation, presented in Fig. 21(b), indicate that the proposed antenna has wideband and high port isolation characteristics at sub-6 GHz. The measurement reported that the impedance bandwidth at $|S_{11}| > 10$ dB was 40% and port isolation is $|S_{21}| > 25$ dB at the central frequency. Therefore, it was confirmed through simulations and measurements that the impedance bandwidth was 40%. The measurement results agreed with those of the simulations.

## REFERENCES

[1] Y. Li, Z. Zhao, Z. Tang, and Y. Yin, "Differentially-fed, wideband dual-polarized filtering antenna with novel feeding structure for 5G sub-6 GHz base station applications," *IEEE Access*, vol. 7, pp. 184718–184725, 2019.

[2] G. S. Karthikeya, S. K. Koul, A. K. Poddar, and U. L. Rohde, "Compact bent-corner orthogonal beam switching antenna module for 5G mobile devices," *J. Electromagn. Eng. Sci.*, vol. 22, no. 1, pp. 74–83, Jan. 2022.

[3] I. Kim and B. Lee, "Wideband antenna for high-frequency 5G wireless communication," *J. Electromagn. Eng. Sci.*, vol. 22, no. 3, pp. 296–301, May 2022.

[4] Y. Li, Z. Zhao, Z. Tang, and Y. Yin, "Differentially fed, dual-band dual-polarized filtering antenna with high selectivity for 5G sub-6 GHz base station applications," *IEEE Trans. Antennas Propag.*, vol. 68, no. 4, pp. 3231–3236, Apr. 2020.

[5] L.-H. Wen, S. Gao, Q. Luo, Q. Yang, W. Hu, and Y. Yin, "A low-cost differentially driven dual-polarized patch antenna by using open-loop resonators," *IEEE Trans. Antennas Propag.*, vol. 67, no. 4, pp. 2745–2750, Apr. 2019.

[6] J. Seo et al., "Miniaturized dual-band broadside/endfire antenna-in-package for 5G smartphone," *IEEE Trans. Antennas Propag.*, vol. 69, no. 12, pp. 8100–8114, Dec. 2021.

[7] H. Kim, J. Kim, and J. Oh, "Liquid-crystal-based X-band reactively loaded reflectarray unit cell to reduce reflection loss," *IEEE Antennas Wireless Propag. Lett.*, vol. 20, no. 10, pp. 1898–1902, Oct. 2021.

[8] J. Oh, "Millimeter-wave thin lens employing mixed-order elliptic filter arrays," *IEEE Trans. Antennas Propag.*, vol. 64, no. 7, pp. 3222–3227, Jul. 2016.

[9] S. Hong, Y. Kim, and J. Oh, "Automobile laminated glass window embedded transmitarray and ray tracing validation for enhanced 5G connectivity," *IEEE Trans. Antennas Propag.*, vol. 70, no. 8, pp. 6671–6682, Aug. 2022.

[10] E. Kim, S.-T. Ko, Y. J. Lee, and J. Oh, "Millimeter-wave tiny lens antenna employing U-shaped filter arrays for 5G," *IEEE Antennas Wireless Propag. Lett.*, vol. 17, no. 5, pp. 845–848, May 2018.

[11] L. Y. Nie et al., "A low-profile coplanar dual-polarized and dual-band base station antenna array," *IEEE Trans. Antennas Propag.*, vol. 66, no. 12, pp. 6921–6929, Dec. 2018.

[12] Y. Gou, S. Yang, J. Li, and Z. Nie, "A compact dual-polarized printed dipole antenna with high isolation for wideband base station applications," *IEEE Trans. Antennas Propag.*, vol. 62, no. 8, pp. 4392–4395, Aug. 2014.

[13] H. Jin, L. Zhu, H. Zou, Y. Luo, S. Xu, and G. Yang, "A wideband dual-polarized antenna and its array with electrically downtilt function for 5G sub-6 GHz communication applications," *IEEE Access*, vol. 8, pp. 7672–7681, 2020.

[14] J. Cho, T. H. Lim, Y. Kim, and H. Choo, "Design of a wideband printed patch dipole antenna with a balanced on-board feeding network," *J. Electromagn. Eng. Sci.*, vol. 22, no. 6, pp. 631–637, Nov. 2022.

[15] J. Oh and K. Sarabandi, "Compact, low profile, common aperture polarization, and pattern diversity antennas," *IEEE Trans. Antennas Propag.*, vol. 62, no. 2, pp. 569–576, Feb. 2014.

[16] K. E. Kolodziej, *In-Band Full-Duplex Wireless Systems Handbook*. Norwood, MA, USA: Artech House, 2021.

[17] T. Zahir, K. Arshad, A. Nakata, and K. Moessner, "Interference management in femtocells," *IEEE Commun. Surveys Tuts.*, vol. 15, no. 1, pp. 293–311, 1st Quart., 2013.

[18] A. Sabharwal, P. Schniter, D. Guo, D. W. Bliss, S. Rangarajan, and R. Wichman, "In-band full-duplex wireless: Challenges and opportunities," *IEEE J. Sel. Areas Commun.*, vol. 32, no. 9, pp. 1637–1652, Sep. 2014.

[19] H. Nawaz, M. A. Basit, and A. U. Niazi, "A compact, dual-polarized patch antenna with improved $T_x$–$R_x$ isolation for 2.4 GHz single frequency full-duplex applications," *Int. J. Microw. Wireless Technol.*, vol. 13, no. 3, pp. 266–273, 2021.

[20] P. V. Prasannakumar, M. A. Elmansouri, and D. S. Filipovic, "Wideband decoupling techniques for dual-polarized bi-static simultaneous transmit and receive antenna subsystem," *IEEE Trans. Antennas Propag.*, vol. 65, no. 10, pp. 4991–5001, Oct. 2017.

[21] C. Wei, Z.-Y. Zhang, and K.-L. Wu, "Phase compensation for decoupling of large-scale staggered dual-polarized dipole array antennas," *IEEE Trans. Antennas Propag.*, vol. 68, no. 4, pp. 2822–2831, Apr. 2020.

[22] Y.-M. Zhang, S. Zhang, J.-L. Li, and G. F. Pedersen, "A wavetrap-based decoupling technique for 45° polarized MIMO antenna arrays," *IEEE Trans. Antennas Propag.*, vol. 68, no. 3, pp. 2148–2157, Mar. 2020.

[23] Y.-M. Zhang, S. Zhang, J.-L. Li, and G. F. Pedersen, "A transmission-line-based decoupling method for MIMO antenna arrays," *IEEE Trans. Antennas Propag.*, vol. 67, no. 5, pp. 3117–3131, May 2019.

[24] C. Lu, Q. Zhang, H. Qi, S. Li, H. Zhao, and X. Yin, "Compact postwall slotline-based stepped impedance resonator decoupling structure for isolation enhancement of patch antenna array," *IEEE Antennas Wireless Propag. Lett.*, vol. 18, no. 12, pp. 2647–2651, Dec. 2019.

[25] S. Hwangbo, H. Y. Yang, and Y.-K. Yoon, "Mutual coupling reduction using micromachined complementary meander-line slots for a patch array antenna," *IEEE Antennas Wireless Propag. Lett.*, vol. 16, pp. 1667–1670, 2017.

[26] K. Wei, J.-Y. Li, L. Wang, Z.-J. Xing, and R. Xu, "Mutual coupling reduction by novel fractal defected ground structure bandgap filter," *IEEE Trans. Antennas Propag.*, vol. 64, no. 10, pp. 4328–4335, Oct. 2016.

[27] Z. Wang, C. Li, and Y. Yin, "A meta-surface antenna array decoupling (MAAD) design to improve the isolation performance in a MIMO system," *IEEE Access*, vol. 8, pp. 61797–61805, 2020.

[28] Z. Wang, L. Zhao, Y. Cai, S. Zheng, and Y. Yin, "A meta-surface antenna array decoupling (MAAD) method for mutual coupling reduction in a MIMO antenna system," *Sci. Rep.*, vol. 8, no. 1, pp. 1–9, Feb. 2018.

[29] S. Kim and S. Nam, "A compact and wideband linear array antenna with low mutual coupling," *IEEE Trans. Antennas Propag.*, vol. 67, no. 8, pp. 5695–5699, Aug. 2019.

[30] Y.-M. Zhang and S. Zhang, "A side-loaded-metal decoupling method for 2 × n patch antenna arrays," *IEEE Antennas Wireless Propag. Lett.*, vol. 20, no. 5, pp. 668–672, May 2021.

[31] L. Sun, Y. Li, Z. Zhang, and H. Wang, "Antenna decoupling by common and differential modes cancellation," *IEEE Trans. Antennas Propag.*, vol. 69, no. 2, pp. 672–682, Feb. 2021.

[32] L. Zhao, K.-W. Qian, and K.-L. Wu, "A cascaded coupled resonator decoupling network for mitigating interference between two radios in adjacent frequency bands," *IEEE Trans. Microw. Theory Techn.*, vol. 62, no. 11, pp. 2680–2688, Nov. 2014.

[33] K.-D. Xu, H. Luyen, and N. Behdad, "A decoupling and matching network design for single- and dual-band two-element antenna arrays," *IEEE Trans. Microw. Theory Techn.*, vol. 68, no. 9, pp. 3986–3999, Sep. 2020.

[34] J. Sui and K.-L. Wu, "A general T-stub circuit for decoupling of two dual-band antennas," *IEEE Trans. Microw. Theory Techn.*, vol. 65, no. 6, pp. 2111–2121, Jun. 2017.

[35] Y.-M. Zhang and S. Zhang, "A novel aperture-loaded decoupling concept for patch antenna arrays," *IEEE Trans. Microw. Theory Techn.*, vol. 69, no. 9, pp. 4272–4283, Sep. 2021.

[36] Y.-F. Cheng and K. M. Cheng, "A novel dual-band decoupling and matching technique for asymmetric antenna arrays," *IEEE Trans. Microw. Theory Techn.*, vol. 66, no. 5, pp. 2080–2089, May 2018.

[37] H. Meng and K.-L. Wu, "An LC decoupling network for two antennas working at low frequencies," *IEEE Trans. Microw. Theory Techn.*, vol. 65, no. 7, pp. 2321–2329, Jul. 2017.

[38] K. Qian, L. Zhao, and K.-L. Wu, "An LTCC coupled resonator decoupling network for two antennas," *IEEE Trans. Microw. Theory Techn.*, vol. 63, no. 10, pp. 3199–3207, Oct. 2015.

[39] M. Niroo-Jazi, T. A. Denidni, M. R. Chaharmir, and A. R. Sebak, "A hybrid isolator to reduce electromagnetic interactions between Tx/Rx antennas," *IEEE Antennas Wireless Propag. Lett.*, vol. 13, pp. 75–78, 2014.

[40] L. Qiu, F. Zhao, K. Xiao, S.-L. Chai, and J.-J. Mao, "Transmit–receive isolation improvement of antenna arrays by using EBG structures," *IEEE Antennas Wireless Propag. Lett.*, vol. 11, pp. 93–96, 2012.

[41] F. Yang and Y. Rahmat-Samii, "Microstrip antennas integrated with electromagnetic band-gap (EBG) structures: A low mutual coupling design for array applications," *IEEE Trans. Antennas Propag.*, vol. 51, no. 10, pp. 2936–2946, Oct. 2003.

[42] K.-L. Wu, C. Wei, X. Mei, and Z.-Y. Zhang, "Array-antenna decoupling surface," *IEEE Trans. Antennas Propag.*, vol. 65, no. 12, pp. 6728–6738, Dec. 2017.

[43] S. Zhang, X. Chen, and G. F. Pedersen, "Mutual coupling suppression with decoupling ground for massive MIMO antenna arrays," *IEEE Trans. Veh. Technol.*, vol. 68, no. 8, pp. 7273–7282, Aug. 2019.

[44] Y.-N. Chen, C. Ding, H. Zhu, and Y. Liu, "A±45°-polarized antenna system with four isolated channels for in-band full-duplex (IBFD)," *IEEE Trans. Antennas Propag.*, vol. 71, no. 4, pp. 3000–3010, Apr. 2023.

[45] J. Li, S. Yang, Y. Gou, J. Hu, and Z. Nie, "Wideband dual-polarized magnetically coupled patch antenna array with high port isolation," *IEEE Trans. Antennas Propag.*, vol. 64, no. 1, pp. 117–125, Jan. 2016.

[46] D. M. Pozar, *Microwave Engineering*. Hoboken, NJ, USA: Wiley, 2011.

[47] D. Wu, S. W. Cheung, Q. L. Li, and T. I. Yuk, "Decoupling using diamond-shaped patterned ground resonator for small MIMO antennas," *IET Microw., Antennas Propag.*, vol. 11, no. 2, pp. 177–183, Jan. 2017.

[48] R. Abhari and G. V. Eleftheriades, "Metallo-dielectric electromagnetic bandgap structures for suppression and isolation of the parallel-plate noise in high-speed circuits," *IEEE Trans. Microw. Theory Techn.*, vol. 51, no. 6, pp. 1629–1639, Jun. 2003.

[49] Y. Li and Q.-X. Chu, "Dual-layer superstrate structure for decoupling of dual-polarized antenna arrays," *IEEE Antennas Wireless Propag. Lett.*, vol. 21, no. 3, pp. 521–525, Mar. 2022.
[50] M. Ciydem and E. A. Miran, "Dual-polarization wideband sub-6 GHz suspended patch antenna for 5G base station," *IEEE Antennas Wireless Propag. Lett.*, vol. 19, no. 7, pp. 1142–1146, Jul. 2020.
[51] R. C. Hansen and M. Burke, "Antennas with magneto-dielectrics," *Microw. Opt. Technol. Lett.*, vol. 26, no. 2, pp. 75–78, 2000.
[52] V. G. Kasabegoudar and K. J. Vinoy, "Coplanar capacitively coupled probe fed microstrip antennas for wideband applications," *IEEE Trans. Antennas Propag.*, vol. 58, no. 10, pp. 3131–3138, Oct. 2010.

**Taeyeong Yoon** (Graduate Student Member, IEEE) received the B.S. degree (summa cum laude) in electronic engineering from Korea Aerospace University, Goyang, South Korea, in 2021, and the M.S. degree from the Department of Electrical and Computer Engineering, Seoul National University, Seoul, South Korea, in 2023, where he is currently pursuing the Ph.D. degree.

His current research interests include suppressing dual-polarized multi-path coupling, dual-polarized antennas for sub-6 GHz applications, high-efficiency power amplifiers for millimeter-wave applications, and RF/mm-wave/microwave-integrated circuits.

**Uichan Park** (Graduate Student Member, IEEE) received the B.S. degree in electronic and electrical engineering from Sungkyunkwan University, Suwon, South Korea, in 2020. He is currently pursuing the integrated master's and Ph.D. degrees at the Department of Electrical and Computer Engineering, Seoul National University, Seoul, South Korea.

His current research interests include behavioral modeling and digital predistortion for RF power amplifiers, and antenna-in-package for millimeter-wave radar systems.

**Jungsuek Oh** (Senior Member, IEEE) received the B.S. and M.S. degrees from Seoul National University, Seoul, South Korea, in 2002 and 2007, respectively, and the Ph.D. degree from the University of Michigan at Ann Arbor, Ann Arbor, MI, USA, in 2012.

From 2007 to 2008, he was with Korea Telecom, Seoul, as a Hardware Research Engineer, working on the development of flexible RF devices. From 2013 to 2014, he was a Staff RF Engineer with Samsung Research America, Dallas, TX, USA, working as a Project Leader for the 5G/millimeter-wave antenna system. He is currently an Associate Professor at the School of Electrical and Computer Engineering, Seoul National University. He has published more than 60 technical journal and conference papers. His research areas include mmWave beam focusing/shaping techniques, antenna miniaturization for integrated systems, and radio propagation modeling for indoor scenarios.

Dr. Oh was the recipient of the 2011-2012 Rackham Predoctoral Fellowship Award, 2014 Samsung DMC R&D Innovation Award, 2018 SNU Creative Researcher Award, 2019 Samsung Electro-Mechanics Silver Prize, and the best paper awards from several conferences. He has served as a TPC Member and as a Session Chair for the IEEE Antennas and Propagation Society/U.S. National Committee-International Union of Radio Science (AP-S/USNC-URSI) and IEEE International Symposium on Antennas and Propagation (ISAP).